THE ASTROPHYSICAL JOURNAL, 514:979–988, 1999 April 1

ACOUSTIC IMAGING IN HELIOSEISMOLOGY

DEAN-YI CHOU AND HSIANG-KUANG CHANG
Physics Department, Tsing Hua University, Hsinchu, 30043, Taiwan, Republic of China
MING-TSUNG SUN
Department of Mechanical Engineering, Chang-Gung University, Kwei-San, 33333, Taiwan, Republic of China
BARRY LABONTE
Institute for Astronomy, University of Hawaii, Honolulu, HI 96822
HUEI-RU CHEN AND SHENG-JEN YEH
Physics Department, Tsing Hua University, Hsinchu, 30043, Taiwan, Republic of China
AND
THE TON TEAM[1]
Received 1997 December 15; accepted 1998 November 6

ABSTRACT

The time-variant acoustic signal at a point in the solar interior can be constructed from observations at the surface, based on the knowledge of how acoustic waves travel in the Sun: the time-distance relation of the *p*-modes. The basic principle and properties of this imaging technique are discussed in detail. The helioseismic data used in this study were taken with the Taiwan Oscillation Network (TON). The time series of observed acoustic signals on the solar surface is treated as a phased array. The time-distance relation provides the phase information among the phased array elements. The signal at any location at any time can be reconstructed by summing the observed signal at array elements in phase and with a proper normalization. The time series of the constructed acoustic signal contains information on frequency, phase, and intensity. We use the constructed intensity to obtain three-dimensional acoustic absorption images. The features in the absorption images correlate with the magnetic field in the active region. The vertical extension of absorption features in the active region is smaller in images constructed with shorter wavelengths. This indicates that the vertical resolution of the three-dimensional images depends on the range of modes used in constructing the signal. The actual depths of the absorption features in the active region may be smaller than those shown in the three-dimensional images.

Subject headings: Sun: magnetic fields — Sun: oscillations — sunspots

1. INTRODUCTION

In conventional helioseismology, most results are obtained from a global mode analysis. A time series of intensity or velocity images is decomposed into eigenmodes, characterized by radial order n, spherical harmonic degree l, and azimuthal order m. Given the dispersion relation of *p*-modes, the eigenfrequencies as a function of n, l, and m provide the global information on the solar interior. Recently interest in studying the local structure of the Sun in helioseismology has grown rapidly because high spatial resolution helioseismic data, such as data from the Taiwan Oscillation Network (TON) (Chou et al. 1995) and the *Solar and Heliospheric Observatory* (*SOHO*) (Scherrer 1995), have become available.

Braun, Duvall, & LaBonte (1987) first decomposed the *p*-mode oscillations around a sunspot into ingoing and outgoing modes to study the interaction of *p*-modes with the sunspot. Hill (1988) used the dispersion relation of *p*-modes derived from a local area (ring diagram) to probe the local subsurface flow. Duvall et al. (1993) first developed a new technique, time-distance analysis, to analyze the helioseismic data. Time-distance analysis is performed directly in the spacetime domain instead of in the frequency-wavenumber domain. It is a useful tool to study the local structure. So far most studies of time-distance analysis are based on finding and interpreting the perturbation of time-distance curves due to local inhomogeneities (Jefferies et al. 1994; D'Silva et al. 1996; Duvall et al. 1996; Kosovichev 1996; Braun 1997; Bogdan et al. 1997; Kosovichev & Duvall 1997; Woodard 1997).

Some authors (Roddier 1975; Lindsey & Braun 1990; Braun et al. 1992) proposed local diagnostics of the solar interior based on acoustic holography. Lindsey & Braun (1997) prescribed computational applications for helioseismic holography from two fairly separate directions: the spectral perspective and the time-distance perspective. Chang et al. (1997, hereafter Paper I) independently developed an acoustic imaging method, based on the time-distance relation, and for the first time constructed a three-dimensional acoustic intensity image of the solar interior with the helioseismic data observed with TON. The constructed time series of acoustic waves includes both intensity and phase information (Lindsey & Braun 1997). Chen et al. (1998) first used phase information to construct a three-dimensional phase map of the solar interior.

In this paper we discuss the basic principle and properties of this acoustic imaging method in detail, and study another data set, also observed with TON, with an improved technique. In § 2 we discuss the basic principle of acoustic

[1] The TON Team includes Heng-Tai Tang, Wei-Cheng Shiu, and Yi-Liang Chen (Physics Department, Tsing Hua University, Hsinchu, 30043, Taiwan); Antonio Jimenez and Maria Cristina Rabello-Soares (Instituto Astrofísica de Canarias, Observatorio del Teide, Tenerife, Spain); Guoxiang Ai and Gwo-Ping Wang (Huairou Solar Observing Station, Beijing Observatory, Beijing, China); Philip Goode and William Marquette (Big Bear Solar Observatory, New Jersey Institute of Technology, Newark, NJ 07102); Shuhrat Ehgamberdiev and Shukur Khalikov (Ulugh Beg Astronomical Institute, Tashkent, Uzbekistan).

imaging. We describe the data reduction procedure in § 3. We discuss the results in § 4 and the properties of acoustic imaging in § 5.

2. BASIC PRINCIPLE

The goal of acoustic imaging is to construct the spatial distribution of the acoustic signal in the solar interior at any time. Here we adopt the idea of the daily experience: imaging an object illuminated by ambient light. The image of an object, illuminated by scattered daylight, is formed by an optical lens. The function of the optical lens is to add the electromagnetic signals from each point on the target object in phase to form the image. The solar p-mode waves, which are continually generated and dissipated stochastically by the turbulent convection, can play the same role as ambient daylight. The p-mode waves are scattered and absorbed by local inhomogeneities. If we appropriately add the p-mode waves observed at the surface such that the acoustic signal emanating from a particular point at a particular time is collected in phase, we can reconstruct the p-mode amplitude at the target point at the target time. The scheme of adding signals from the target point in phase plays the same role as a lens in optics.

The idea of phased-array imaging is an old one, and is most familiar in astronomy in radio interferometry. Dedicated solar phased arrays (Wild 1961; Nakajima et al. 1980) produce two-dimensional snapshot images of solar structures. The concept has wide use in radar and sonar applications as well as in astronomy. The pressure fluctuations in the sound waves that impinge upon every point on the solar surface cause detectable fluctuations in the temperature and velocity of the surface. Every spatial point can therefore be used as an element of a hydrophone array. Phasing the time signals from the various elements produces the image.

The solar p-mode waves are different from the daylight. In the Sun, p-modes propagate in an inhomogeneous, anisotropic, and dispersive medium. Different p-modes propagate differently in the Sun and have different propagators. A resonant p-mode is trapped and multiply reflected in a cavity between the surface and a layer in the solar interior. The acoustic signal emanating from a point at the surface propagates downward to the bottom of the cavity and back to the surface at a different horizontal distance from the original point. Different p-modes have different paths and arrive at the surface with different times and different distances from that point.

However, Duvall's law (Duvall 1982) greatly simplifies the description of p-mode propagation in the Sun. The modes with the same angular phase velocity ω/l have approximately the same ray path, where ω is the mode frequency. They form a wave packet which carries the signal from point to point in the Sun. The relation of the travel time and the angular distance traveled by the wave packet can be measured with a cross-correlation technique (Duvall et al. 1993). Each point on the time-distance curve corresponds to a wave packet formed by the modes with the same ω/l. It is noted that the computed time-distance relation from a standard solar model based on the ray theory at 3 mHz agrees well with the observed one (D'Silva & Duvall 1995).

Suppose we want to reconstruct the wave amplitude at ($\boldsymbol{r}$, t), where $\boldsymbol{r}$ can be any point in the Sun. Initially, we assume that $\boldsymbol{r}$ is on the surface. The p-modes emanating from ($\boldsymbol{r}$, t) can be grouped into different wave packets characterized by the angular phase velocity ω/l. Different wave packets bounce back to the surface at different ($\boldsymbol{r}'$, t'). If we can collect the acoustic signals measured at all ($\boldsymbol{r}'$, t') based on the knowledge of how acoustic waves travel in the Sun, the time-distance relation, in principle we can reconstruct the acoustic wave amplitude at ($\boldsymbol{r}$, t). If we treat the time series of observed images as the temporal signal detected on a phased array, the time-distance curve provides the phase information among the phase elements. Summing the observed amplitude at array elements in phase and normalized with an appropriate weighting function, we can reconstruct the acoustic amplitude at the target point $\boldsymbol{r}$ at the target time t.

Since the travel time depends on the angular distance from the target point, the signals at the angular distance Δ from the target point are averaged to obtain the azimuthal-averaged amplitude $\bar{\Psi}(\Delta, t)$ in the first step of the coherent sum in acoustic imaging. Azimuthal averaging isolates only the modes with $m = 0$, which propagate only inward toward the target point or outward from the target point. The signal originating from a target point at time t is constructed by summing the azimuthal-averaged amplitudes at different angular distances from the target point measured at the appropriate time delays based on the time-distance curve

$$\Psi_c(t) = \sum_{\tau=\tau_1}^{\tau_2} W\bar{\Psi}(\Delta, t+\tau)\,, \tag{1}$$

where $\Psi_c(t)$ is the constructed signal at the target point at t, $\bar{\Psi}(\Delta, t+\tau)$ is the azimuthal-averaged signal at a distance Δ from the target point at time $t+\tau$, and τ is determined from the time-distance curve obtained from the quiet Sun. The summation variable τ is evenly spaced in the interval (τ_1, τ_2). The factor $W \propto (\sin\Delta/\tau^2)^{1/2}$ is the weighting function to account for different weights for different wave packets. For a polytropic atmosphere, $(\sin\Delta/\tau^2)^{1/2} \propto (\sin\Delta/\Delta)^{1/2}$. In the limit of small angle, this weighting function is equivalent to that which equation (4) of Braun et al. (1998) prescribes for proper, single-skip egression computations in a plane-parallel polytrope for shallow focal planes. Thus the coherent sum in equation (1) is practically equivalent to the egression in an acoustic holograph. It is noted that the summation in the egression in Braun et al. (1998) is evenly over the solar surface. There is a conversion factor between the summation over space in the egression of Braun et al. and the summation over time in equation (1).

To construct the acoustic amplitude at a point below the surface, we need to focus our acoustic array on this subsurface target point. This requires the time-distance relation between a subsurface point and a surface point. Equation (1) is still valid, but now τ is the travel time from the subsurface target point to the observing points on the surface at an angular distance Δ from the target point. Since the time-distance relation between a subsurface point and a surface point cannot be obtained from observations, we have to compute it from a standard solar model, using the ray approximation (J. Christensen-Dalsgaard 1990, private communication; D'Silva & Duvall 1995). The good agreement between the computed time-distance relation and the observed one for the surface justifies using the computed time-distance relations for subsurface targets. The computed time-distance curves at a wave frequency of 3 mHz are shown in Figure 1 for various focal depths. Those curves

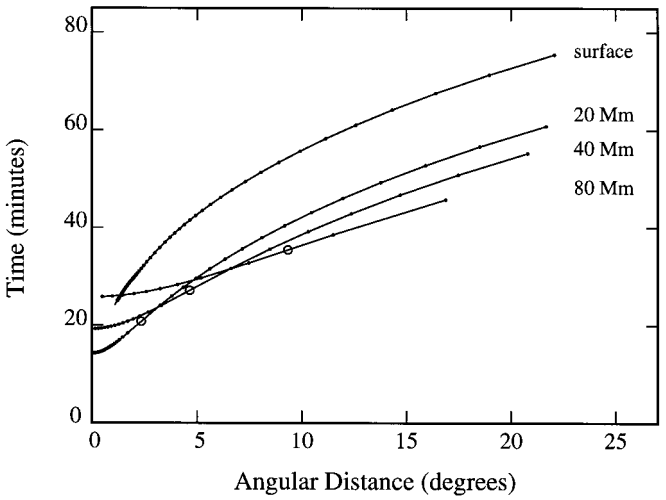

FIG. 1.—Time-distance relations at various focal depths, computed from a standard solar model, based on ray theory, at 3 mHz. For each curve, the filled circles correspond to modes whose l is a multiple of 10, starting with $l = 80$ at the right end of each curve. The highest-l mode which can penetrate into the depth of the target point is marked by an open circle on each curve. The l value decreases going in either direction away from the l_{max} point along the curve.

are for rays that do not reflect from the surface before reaching the point of detection. Waves that are reflected between the target and the point of detection have longer travel times, and an analogous set of time-distance curves can be computed. To distinguish among these different sets of rays, the convention is to identify the rays by the number of upward passages between target and detection. The curves in Figure 1 thus are for single-bounce rays. Rays with one reflection between target and detection are two-bounce, and so on.

Each point (Δ, τ) on a time-distance curve corresponds to the modes having the same ω/l, which form a wave packet. For the surface time-distance curve, this wave packet takes time τ to travel between two surface points separated by an angular distance Δ. At a particular frequency, 3 mHz for example, each point on the curve corresponds to one l-value. A mode of lower l travels a larger Δ as it emerges to the surface again. Thus, for the time-distance curve at the surface, l decreases along the curve as Δ increases. For example, $\Delta = 2°$ corresponds to $l = 386$, and $\Delta = 14°$ corresponds to $l = 112$ for $\omega = 3$ mHz. For each curve in Figure 1, the filled circles correspond to modes whose l is a multiple of 10, starting with $l = 80$ at the right end of each curve.

The situation is more complicated for the time-distance relation between a subsurface target point and a surface observation point. If the target point is at a depth D below the surface, as sketched in Figure 2, it is inaccessible to p-modes that have turning depths shallower than the target depth. At a constant frequency, the modes with l higher than l_{max} cannot penetrate into the depth of the target point. For example, at 3 mHz $l_{max} = 230$, 147, and 92 for $D = 20$, 40, and 80 Mm, respectively. In Figure 2, point A is the target point, and CAF corresponds to the ray path of the l_{max} mode, which has a turning depth equal to the target depth. The point corresponding to l_{max} on the time-distance curve is a reflection point, whose location is marked by an open circle in Figure 1. Paths AG and AE correspond to the same ω/l. But they have the different locations on the time-distance curve. On the time-distance curve, path AG corresponds to a point on the right-hand side of the l_{max} point, and path AE corresponds to a point on the left-hand side of the l_{max} point. The l-value decreases going in either direction away from the l_{max} point along the curve.

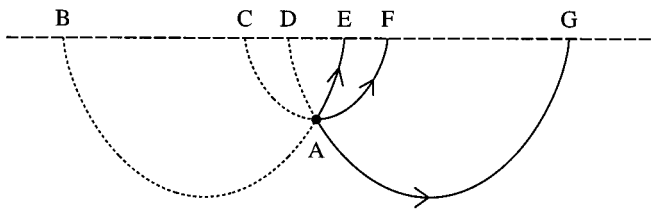

FIG. 2.—Sketch of the ray paths for different modes with the same ω/l. Point A is the target point. The ray path CAF corresponds to the l_{max} point on the time-distance curve. Wave packets from B and D pass the target point A and reach the surface at E and G, respectively. These two wave packets have the same ω/l. Point E corresponds to a point on the left-hand side of the l_{max} point on the time-distance curve in Fig. 1, and point G corresponds to a point on the right-hand side.

3. OBSERVATIONS AND DATA REDUCTION

The helioseismic data used in this study were taken with the TON instruments in Tenerife, Big Bear, and Tashkent. A discussion of the TON project and its instruments is given by Chou et al. (1995). The TON data are full-disk K-line images recorded by a 16 bit 1080 × 1080 water-cooled CCD. The images are taken at a rate of one image per 60 s. The diameter of the Sun is about 1000 pixels. The measured amplitude of intensity oscillations is about 2.5%.

The time series in this study is 1996 August 1–3. We select NOAA 7981, which is a large old active region, as the target region. The preceding sunspot has little change, while the several following sunspots change significantly during this period. The latitude of the preceding sunspot is about 10°south in the Carrington coordinates.

The preliminary data reduction of the TON data, such as flat-fielding and registration, is given by Chen, Chou, & the TON Team (1996). The data reduction procedure to construct solar acoustic images at various focal depths is described as follows:

1. The limb darkening of the K-line intensity image is removed.
2. Each observed K-line full-disk image is transformed into $\sin\theta$–ϕ coordinates with the GRASP package developed by GONG, where θ and ϕ are the latitude and the longitude, respectively, in a spherical coordinate system aligned along the solar rotation axis. In $\sin\theta$–ϕ coordinates, the range $-1 < \sin\theta < 1$ and $-90° < \phi < 90°$ corresponds to 512 × 512 pixels.
3. The solar differential rotation at the surface is removed with an observed surface differential rotation velocity (Libbrecht & Morrow 1991). This issue is discussed in § 5.5.
4. Aperiodic variation is suppressed by subtracting the 15 frame running mean from the intensity time series at each spatial point. This introduces aliasing below a frequency around 1.11 mHz, but the following temporal filter will remove this aliasing.
5. The signal in a range of 2.7–6.5 mHz is isolated with the Fourier transform.
6. The signal inside the sunspot is set to zero because scattered light contaminates the measurement and slight misregistration introduces a spurious signal.

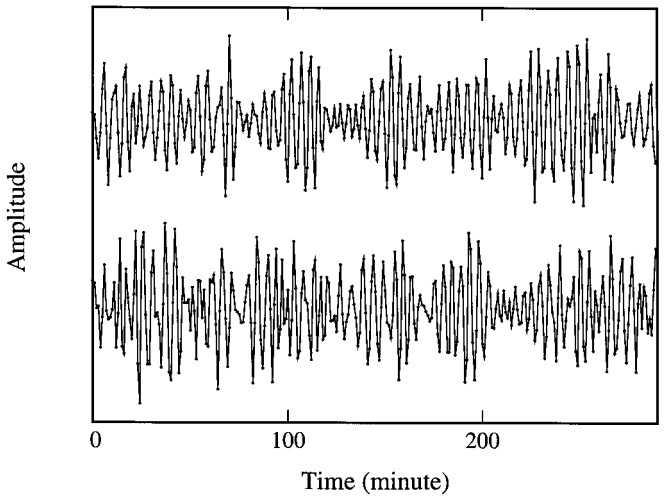

FIG. 3.—Time series of the observed amplitude (*lower graph*) and the time series of amplitude constructed with outgoing wave (*upper graph*) for a target point in the quiet Sun. The amplitude scale is arbitrary. The phase of the constructed series is ahead of the observed phase by about 1 minute, measured from the cross-correlation of the two signals.

7. The signals at the angular distance Δ from the target point are averaged to obtain the azimuthal-averaged amplitude $\bar{\Psi}(\Delta, t)$. The signal at the target point at time t is constructed based on equation (1).

8. In this study we use two different annular collecting areas (apertures), corresponding to different l-ranges, to construct the acoustic signal at the target point. The smaller angle aperture is 2°–5°.5, corresponding to $l = 202$–378 at 3 mHz for the surface. The larger angle aperture is 2°–14°, corresponding to $l = 112$–378 at 3 mHz for the surface. In the measurements made using the small-angle aperture, we find that the intensity maps constructed by the ingoing waves with one-bounce time-distance curve show ghost images near the sunspots which are caused by inaccurate signals measured in the sunspots (the observed signal in the sunspot is set to zero in data processing). Thus we use a two-bounce time-distance curve for the small-angle aperture to avoid the effect of the sunspots. The effects of aperture choice are discussed in §§ 5.6 and 5.7.

9. The phased summation is repeated for each t in the time series. The time series of constructed amplitude at a target point in the quiet Sun is shown in Figure 3 (*upper graph*). For comparison, the amplitude observed at that point is also shown in Figure 3 (*lower graph*). The 5 minute oscillations are obvious. The correlation between constructed and observed time series is apparent and will be discussed in § 4. The time series of constructed amplitude contains information on the frequency, the intensity, and the phase of the wave train (Chen et al. 1998). In this study we concentrate on the intensity and only briefly mention phase information.

10. The amplitudes at different t-values are squared and added to obtain the acoustic intensity received from the target point.

11. The procedure is repeated by shifting the aperture to center on each point in a target region, forming a two-dimensional acoustic image. The data from each observing station on each day, defined as one unit, is analyzed separately. The final constructed intensity map is the sum over seven units in the period 1996 August 1–3.

12. The same procedure is applied to construct acoustic images at various focal depths with the time-distance curves for different focal depths.

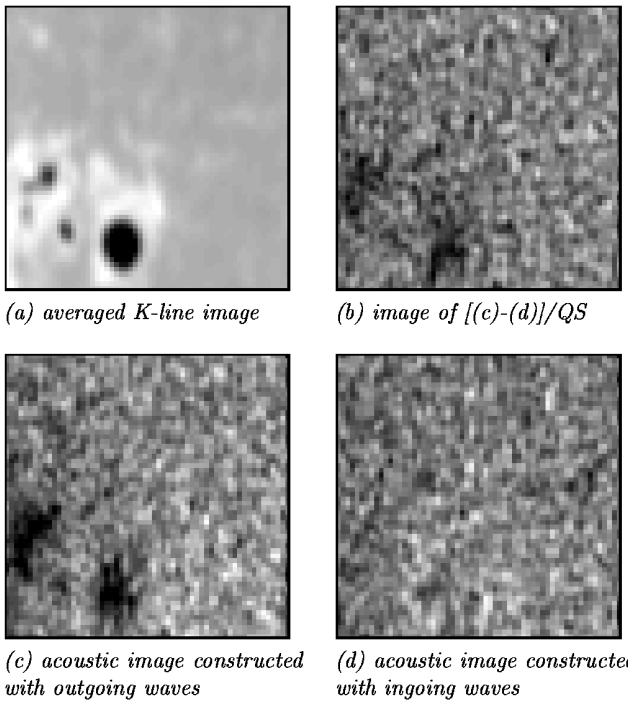

(a) averaged K-line image *(b) image of [(c)-(d)]/QS*

(c) acoustic image constructed with outgoing waves *(d) acoustic image constructed with ingoing waves*

FIG. 4.—(*a*) K-line image and (*c*, *d*) reconstructed acoustic intensity images at the surface for the same area. The K-line intensity image in (*a*) is averaged over the 3 days of observation. The plage structure is blurred by evolution. Image (*c*) is constructed from outgoing waves, and (*d*) is constructed from ingoing waves from the whole observing period. It is apparent that there is no sunspot signature in (*d*); (b) is obtained by subtracting (*d*) from (*c*) and dividing by the average over the quiet region of (*d*). The horizontal (ϕ) and vertical (sin θ) dimensions are 21°.1, and 13°.3, respectively. Thus the aspect ratio is about 3/2, and noise fluctuations in the quiet Sun appear elongated in the north-south direction. The area is selected to include both active and quiet regions.

The constructed acoustic image at the surface from the large-angle collecting area is shown in Figure 4*c*. The dimensions of the target region are 60 × 60 pixels, corresponding to 21°.1 in ϕ (horizontal) and 13°.3 in θ (vertical). Thus its aspect ratio is about 3/2, and features in the quiet Sun appear elongated in the north-south direction. The target region is selected such that both active and quiet regions are included. For comparison, Figure 4*a* shows the corresponding averaged observed K-line intensity image. The K-line intensity image in Figure 4*a* is averaged over the 3 days of observation. The blurred plage structure is caused by evolution during the observing interval. The correspondence between the reconstructed image, Figure 4*c*, and the K-line image, Figure 4*a*, is apparent inside and near the sunspot where the p-mode absorption is strong. The correspondence is less clear in the plage regions where the absorption is weak. We believe that the major component of the spatial fluctuation of acoustic intensity in the quiet Sun shown in Figure 3*c* is noise rather than solar signal. It will be discussed in § 5.2.

4. RESULTS

The constructed acoustic intensity discussed above is the acoustic intensity propagating outward from the target point, since it is constructed by the outgoing waves. We can

also construct the acoustic intensity at a target point by the waves propagating inward from the surrounding area if we use a time-reversed time-distance curve. The time-reversed time-distance curve can be obtained simply by mirror-reflecting the ordinary time-distance curve with respect to the $t = 0$ axis. It corresponds to replacing τ in equation (1) by $-\tau$. The time-reversed time-distance relation describes the waves propagating inward toward the target point ($\boldsymbol{r}$, t) from the surrounding observing points ($\boldsymbol{r}'$, t'). The acoustic image constructed with the time-reversed time-distance curve is shown in Figure 4*d*. It shows several important phenomena: (1) It shows no signature of the sunspot as expected because the ingoing waves in the surrounding area have not been affected by the local properties of the target point before they reach the target point (Paper I). (2) The average ingoing acoustic intensity in the quiet Sun is very close to the average outgoing acoustic intensity. (3) There is no correlation between the spatial fluctuations of the constructed intensity of the quiet Sun for Figures 4*c* and 4*d*. This indicates that the spatial fluctuation may be noise rather than the steady solar signal.

The degree of success in reconstructing the acoustic signal can be measured from the correlation between the reconstructed time series and the observed time series for a target point at the surface (T. L. Duvall, Jr. 1997, private communication). We computed the cross-correlation between the time series of observed acoustic amplitudes at the surface and, separately, the time series reconstructed from ingoing and outgoing waves. Both give a maximum cross-correlation value about 0.4–0.5 for a 400 minute time series. There is also a phase shift between the time series. The phase of the time series constructed with the outgoing waves is ahead of the measured series by about 1 minute, and the phase of the time series constructed with the ingoing waves is behind the measured series by about 1 minute, in the quiet Sun. The phase shifts indicate the phase of the wave train advances about 1 minute after one bounce (Chen et al. 1998).

The acoustic intensity shown in Figures 4*c* and 4*d* is slightly nonuniform in the east-west direction. This is caused by the center-to-limb variation of the *p*-mode oscillatory amplitude in K-line measurements. In the direct acoustic power image, which is computed by summing the squared amplitude of the *p*-mode oscillations, the acoustic power increases in going from the disk center to the limb. This observational effect will cause the nonuniformity in constructed images if the target region is close to the limb in the sense that the west part of the constructed images will be enhanced, as the target region is close to the west limb. In our time series, the data coverage is better, as the target region is in the west part of the solar disk. This accounts for the higher acoustic intensity in the west part (*right-hand side*) of Figures 4*c* and 4*d*. The nonuniformity in the constructed images becomes more apparent as one goes deeper because the low-l modes have the greater contribution as one goes deeper.

We subtract the ingoing acoustic intensity (Fig. 4*c*) from the outgoing intensity (Fig. 4*d*) and then divide the difference by the average of the ingoing acoustic intensity over the quiet Sun for each target point to obtain the fraction of ingoing wave power absorbed by the medium along the wave path. A dark area (negative value) indicates that the acoustic waves are absorbed at the target point and along the wave paths from the target point to the observing points. This is related to the absorption coefficient in other studies (Braun et al. 1987; Bogdan et al. 1993; Chen, Chou, & the TON Team 1996). The absorption image is shown in Figure 4*b*, which is a better way to present the acoustic inhomogeneity, although its noise is higher than the intensity images in Figures 4*c* and 4*d*. Thus we will use it to present the local acoustic inhomogeneity below the surface. The spatial nonuniformity discussed above is removed in the absorption images. The strongest absorption, about 34% for the large-angle aperture, occurs in the preceding sunspot. It is about 4 times the standard deviation of the spatial fluctuation in the quiet Sun. The absorption in the sunspot is weaker than that measured with the mode decomposition method (Braun et al. 1987; Chen, Chou, & the TON Team 1996). This may be due to the lower l modes used in imaging the absorption images. For example, the aperture 2°–14° corresponds to $l = 112$–386 at 3 mHz for the surface (see Fig. 2).

One of the major goals of acoustic imaging is to construct the acoustic intensity image below the surface to study the inhomogeneity in the solar interior. The acoustic intensity at a focal depth can be constructed with the time-distance curve for that focal depth. Figure 2 shows the time-distance curves for several focal depths. To study the inhomogeneity below the surface in the target region, we construct absorption images for focal depths 0–40 Mm at intervals of 10 Mm. The absorption images constructed by outgoing waves at different depths for the large-angle aperture (*left column*) and the small-angle aperture (*right column*) are shown in Figure 5.

Figure 5 shows that the vertical extension of the absorption features in the active region is smaller in the images made from the small-angle aperture. The fraction of acoustic absorption averaged over the umbra and penumbra of the preceding sunspot is shown in Figure 6. The absorption values measured with the small-angle and large-angle apertures are similar (about 16%) at the surface. But the small-angle absorption decreases with focal depth more rapidly than the large-angle absorption. This indicates that the vertical spatial resolution of the three-dimensional absorption images depends on the range of modes used in constructing the signal. The vertical resolution is smaller in the smaller angle aperture because of the shorter wavelengths. The appearance of the absorption feature over a great range of depths in Figure 5 may be exaggerated over their true depths. Braun et al. (1998) suggested that the absorption region is quite superficial. Until the vertical resolution can be quantified, it is premature to identify the actual vertical extension of absorption features in the active region based on these three-dimensional absorption images.

For comparison, we should mention the results from another study with a completely different method, where the absorption of *p*-modes in the sunspot is described by an interaction parameter and the interaction parameter is obtained by inverting the measured absorption coefficients of *p*-modes in sunspots (Chen, Chou, & the TON Team 1997). In that study, the depth dependences of the interaction parameter for two sunspots (NOAA 5254 and NOAA 7887) are similar: they increase rapidly, as going deeper, to a maximum value at a depth of about of 7 Mm and then gradually drop to zero at a depth of about 28–35 Mm.

The absorption images made from the small-angle aperture are sharper and have a smaller fluctuation length scale

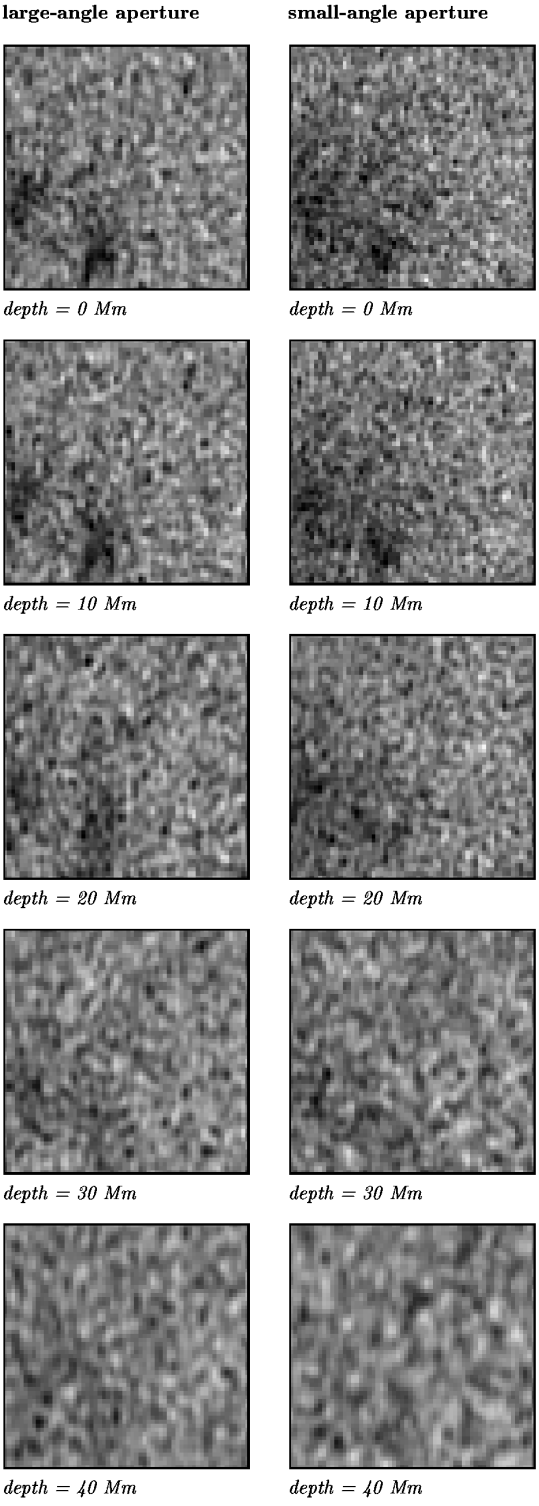

FIG. 5.—Absorption images at various focal depths. The images in the left-hand column are constructed with the 2°–14° aperture, and the images in the right-hand column are constructed with the 2°–5°.5 aperture. The dimension of each image is the same as in Fig. 4.

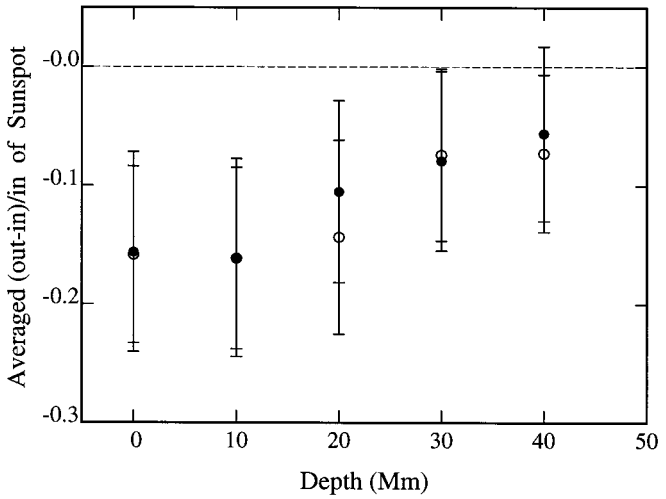

FIG. 6.—Fraction of acoustic absorption averaged over the umbra and penumbra vs. focal depth. Open circles denote the absorption measured with the large-angle aperture. Filled circles denote the absorption measured with the small-angle aperture. The error bar shown here is not the error associated with the average absorption in the sunspot; instead, it is the standard deviation of the spatial fluctuation of the quiet region.

in the quiet Sun. This is because the small-angle aperture corresponds to smaller horizontal wavelengths. The images made from the small-angle aperture are noisier. For example, the standard deviation of the spatial fluctuation of the quiet Sun is 0.084 for the small-angle aperture and 0.075 for the larger angle aperture. There are two possible sources of higher noise. First, the acoustic signal constructed with the small-angle aperture has lower power because the shorter wavelengths have lower power in the acoustic spectrum. Second, the leftover from cancellation of undesired modes over the small aperture is greater.

5. DISCUSSION OF ACOUSTIC IMAGING

5.1. *Absorption, Emission, and Suppression of p-Modes*

It is important to understand the role of the absorption and emission of p-modes in acoustic imaging in order to interpret the constructed acoustic intensity and absorption images. Absorption and emission do not play symmetric roles in acoustic imaging as in the conventional normal mode analysis. First we discuss the acoustic intensity constructed with the outgoing waves. As a wave packet travels from the target point $\boldsymbol{r}$ to the observing point $\boldsymbol{r}'$, the absorption and dissipation at the target point and along the wave path reduce the wave amplitude. The constructed intensity is smaller than the observed intensity at the target point owing to the dissipation and absorption along the wave path. But the emission at the points along the wave path does not contribute to the constructed intensity because it is not at the focal point and the emission is not picked up by the coherent sum. Only the emission at the target point (focal point) contributes to the constructed acoustic intensity.

For the acoustic intensity constructed with the ingoing waves, neither the absorption nor the emission at the target point and along the wave path appears in the constructed intensity. But the observed acoustic intensity at the target point should be lower than the constructed intensity, because of the dissipation and absorption along the wave path from $\boldsymbol{r}'$ to $\boldsymbol{r}$. The absorption images in Figure 5 are computed by subtracting the intensity constructed with the ingoing waves from the intensity constructed with the outgoing waves and then dividing by the ingoing intensity. Thus the absorption image consists of three parts: (1) the absorption and dissipation (negative value) at the target point, (2) the absorption and dissipation (negative value)

along the wave path from $\mathbf{r}'$ to $\mathbf{r}$ and back to $\mathbf{r}'$, and (3) the emission (positive value) at the target point.

From the above discussion, the low-intensity features in images constructed with outgoing waves are due to the absorption at the target point and along the wave path. They are not caused by the suppression of wave amplitude at the target point due to local magnetic field or the local density change. The suppression of wave amplitude at the target point cannot be detected by a coherent sum of signals in the surrounding area because the local suppression disappears as the waves travel to the surrounding area. On the other hand, the local suppression will appear in direct acoustic power maps (Braun et al. 1992). The same argument applies to the local enhancement of the waves.

Since the absorption image contains information on emission as well as absorption of p-modes, it may be a useful tool to study the p-mode emission. For the resonant modes in our study, the lifetime is rather long. The acoustic emission is small relative to the acoustic intensity at each point. By contrast, modes above the cutoff frequency will escape the Sun when they reach the surface. Thus we expect that for the modes above the cutoff frequency the emission relative to the acoustic intensity at each point may be greater and more easily detected.

5.2. *Spatial Fluctuation of Acoustic Intensity in the Quiet Sun*

We believe that the major component of the spatial fluctuation of constructed intensity in the quiet Sun in Figures 4 and 5 is noise, not solar signal. First, there is no correlation between the observed acoustic intensity and the constructed outgoing intensity (Fig. 4*c*) in the quiet Sun. Second, the standard deviation of the spatial fluctuation in the quiet Sun, σ, is approximately inversely proportional to the square root of the data length as shown in Figure 7. The slope of the fitted line in the logarithmic plot is -0.42. Note that σ is computed over the quiet Sun in the target region, which excludes the sunspot and plage area. It is difficult to identify the source of noise. It may include the incomplete cancellation of signals from points other than the target point (see § 5.9), or the variation of the time-distance relation, or the variation of excitation and dissipation of p-modes. Based on the issues discussed in § 5.1, the spatial fluctuation is unlikely to reflect the local acoustic structure at the target points. It could be caused by the local acoustic structure at observing points in the collecting aperture.

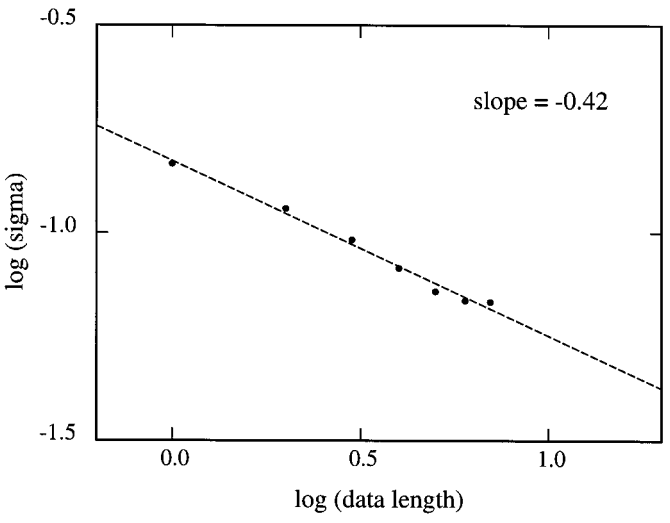

FIG. 7.—Plot of log σ vs. log (data length), where σ is the standard deviation of the spatial fluctuation in the quiet Sun and the data length is in arbitrary units. The slope of the fitted line is -0.42, close to -0.5.

5.3. *Normalization, Weighting, and Apodization*

As discussed in § 2, the weighting function W in equation (1) is proportional to $(\sin \Delta)^{1/2}\Delta^{-1/2}$, which accounts for the different weights for different wave packets. In our previous studies (Paper I; Chen et al. 1998; Chou et al. 1998), we used different weighting functions, which overestimated the lower l components and yielded a poorer spatial resolution in constructed images.

The degree of success in reconstructing the acoustic signal at a target point can be quantified from the correlation between the reconstructed time series and the measured time series for a surface point. Chou et al. (1998) have computed the correlation between the reconstructed and measured time series averaged over the quiet Sun for various test weighting functions and apertures. It shows that the weighting function $(\sin \Delta)^{1/2}\Delta^{-1/4}$, instead of $(\sin \Delta)^{1/2}\Delta^{-1/2}$, has the highest correlation. The cause of this discrepancy is unknown. The study of Chou et al. (1998) shows that the signal constructed with a larger aperture has a higher correlation because larger angle apertures collect a greater range of l in the acoustic power spectrum.

5.4. *Modification of the Time-Distance Curve in Sunspots*

We used the time-distance relation for the quiet Sun to construct the acoustic intensity in both quiet and magnetic regions. Magnetic fields and mass flows in the active region will change the time-distance relation. The change in total travel time between a sunspot and the quiet Sun is about 0.2 minutes (Braun 1997), which is much smaller than the period of p-mode waves. Moreover, it is the differential travel time, not the total travel time, that matters in constructing the intensity (see § 5.6). The differential travel time is the difference of travel time of two adjacent points on the time-distance curve. It is expected that the presence of magnetic field in the active region introduces a change in differential travel time much smaller than the change in total travel time. Thus we believe that using the time-distance relation in the quiet Sun to construct the acoustic intensity in the sunspot is a fairly good approximation. However, the change in travel time will affect the phase of the constructed wave amplitude, and this effect can be detected with the phase measurement (see §§ 5.6 and 5.11).

5.5. *Effect of the Solar Differential Rotation*

The solar differential rotation will modify the wave path. Although the travel time of a wave packet is not affected by the solar rotation, the rotation will change angular distance traveled by the wave packet. In the phase summation, we assume the signal originating from the target point has the same phase on a ring centered at the target point. Thus the differential rotation, including both the latitudinal and the radial differential rotation, will affect the result. In our analysis, we remove only the latitudinal differential rotation on the surface because the radial differential rotation in the convection zone at a fixed latitude is rather small (Libbrecht & Morrow 1991). The radial differential rotation causes a change in the travel distance by less than 1% of the wavelength in the range of interest.

5.6. *Spatial Resolution*

The spatial resolution, in both horizontal and vertical dimensions, is an important issue but difficult to quantify in acoustic imaging. Here we will give a qualitative discussion. As in optics, the spatial resolution of the acoustic imaging technique depends on the wavelength of acoustic waves. For the solar acoustic p-modes, the wavelength is described by l and n. Each point on the time-distance curve represents the modes having the same ω/l. These modes have the same path and form a wave packet. For the target point at the surface, a larger ω/l corresponds to a larger angular distance and longer travel time. For the target point below the surface, at a fixed frequency, ω/l is minimum at the $l_{\max}$ point on the time-distance curve, and increases in both directions along the time-distance curve. The range of time-distance curve used to construct the acoustic image, corresponding to the size of the aperture, determines the range of p-modes used to construct the image. Thus the size of the aperture determines the spatial resolution of the constructed image. The horizontal spatial resolution is determined by l. But the vertical spatial resolution depends on both n and l because the vertical wavelength depends on the depth of the mode cavity, which is determined by l, and the number of radial nodes n. At a single frequency, a smaller angle aperture (smaller ω/l), corresponds to a larger l, and will yield a better horizontal spatial resolution. For a fixed aperture (fixed ω/l), a higher frequency corresponds to a higher n and higher l, and will yield a better vertical and horizontal spatial resolution. The smaller vertical extension of the absorption features in the images made with smaller angle aperture in Figure 5 shows the effect of l on the vertical resolution.

Figure 5 shows that the horizontal spatial resolution of the constructed images becomes poorer at greater focal depth. This can be understood as follows: First, higher l modes cannot penetrate into deep layers; only lower l modes are used to image the deep layers. Second, the time-distance curve is flatter with increasing focal depth. The phase gradient over the observing annulus decreases. The difference in phase used to image adjacent spatial points becomes smaller. This implies that the target point is imaged with a broader point-spread function. Thus the horizontal spatial resolution becomes poorer.

The vertical spatial resolution of constructed acoustic images is more complicated than the horizontal spatial resolution. It depends not only on the wavelength in the vertical direction but also on the change of the shape of the time-distance curve with focal depth. As mentioned in § 5.4, the differential travel time instead of the total travel time plays the role in constructing acoustic intensity. For example, if the time-distance curve in the range of interest is simply shifted upward by a constant time $\delta\tau$, the constructed time series of acoustic amplitude will be identical except for being shifted by $\delta\tau$ in time. The constructed acoustic intensity will be identical because the intensity is the time integral of the squared amplitude (but $\delta\tau$ will affect the phase measurement discussed in § 5.11). Thus the vertical spatial resolution is also determined by the change of the slope of the time-distance curve with focal depth. Figure 1 shows that the slope of time-distance curves has a significant change with focal depth only in the range of small angular distance. Using the small-angle aperture to image will improve the vertical spatial resolution.

We speculate that the small change in the slope of the time-distance curve with focal depth is one of the major effects on the vertical spatial resolution of the intensity maps. As we go from the large-angle aperture to the small-angle aperture, the improvement in the vertical resolution of the intensity maps is less than that of the phase maps (Chen et al. 1998). The vertical resolution of the phase maps is not affected by the small change in the slope of the time-distance curve (see § 5.11).

5.7. *Angular Size of the Phase Array and View Angle*

In our first attempts at coherent summation, the phased array was averaged over 360° about the target point. This restricts our choice of targets to be near the center of the visible disk. It is interesting to consider using a phased array that looks outside of itself, perhaps beyond the limb. We can test the effect of this idea on the spatial resolution by using portions of our annular array. If the phased array is summed over only a certain range of angle (view angle), the horizontal spatial resolution will change. Figure 8 shows images constructed from different view angles and different directions. The images are compressed in the north-south direction to make the aspect-ratio unit. The data set used here is only 512 minutes, so the absorption image of the sunspots is not clear. Figure 8*a* is constructed with a view angle of 360°. Figure 8*b* is constructed with a view angle of 180° from the west (*right*). Figure 8*c* is constructed with a view angle of 180° from the north (*top*). Figure 8*d* is constructed with a view angle of 90° from the north (*top*). From these images, we draw two conclusions: (1) the spatial resolution becomes poorer in the view direction, and (2) the spatial resolution in both directions becomes poorer, as the view angle (effective aperture) becomes smaller (compare Figs. 8*c* and 8*d*). This result is just the same as imaging in electromagnetic waves.

5.8. *Multiple Bounces*

In this study we use the one-bounce time-distance curve for the large-angle aperture and two-bounce time-distance curve for the small-angle aperture. The weighting function

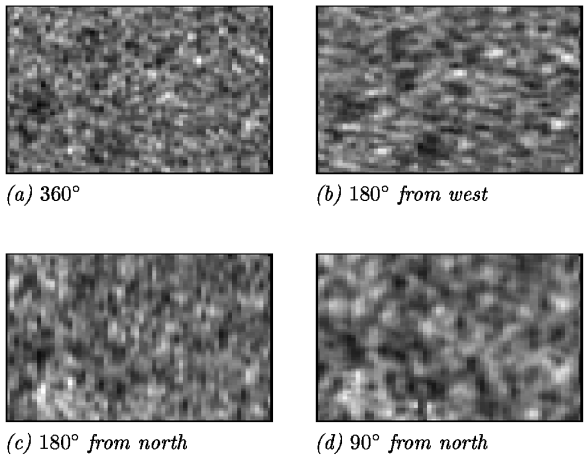

FIG. 8.—Images constructed from different view angles and different directions. The data used here consist of a 512 minute time series. Image *a* is constructed with a view angle of 360°. Image *b* is constructed with a view angle of 180° from the west (*right*). Image *c* is constructed with a view angle of 180° from the north (*top*). Image *d* is constructed with a view angle of 90° from the north (*top*). The images are squeezed in the north-south direction to make the aspect ratio unity.

for the sth-bounce is $W \propto s(\sin s\Delta/s\Delta)^{1/2}$. In the limit of small angle and considering the conversion between different summations, it can be shown that the weighting function multiple bounce used here is equivalent to the weighting function in equation (4) in Braun et al. (1998).

One can add the signals of multiple bounces to enhance the signal-to-noise ratio. But one has to be cautious when adding the signals from multiple bounces because the phases of the time series of amplitude constructed with different bounces are different. The phase of the time series of amplitude constructed from $s + 1$ bounces is about 1.3 minutes ahead of that from s bounces in the quiet Sun (Chen et al. 1998). The correlation value between the time series from one bounce and two bounces is about 0.6 for 385 minute time series. The averaged acoustic intensity over the quiet Sun from two bounces is smaller than that from one bounce by about 6%. The spatial fluctuations of acoustic intensity in the quiet Sun for one bounce and two bounces are very close.

There are two ways to add the signals from different bounces: the incoherent sum and the coherent sum. For the incoherent sum, we simply add the intensities from different bounces. For the coherent sum, we match the phases (shifted by 1 minute) before adding the amplitudes, and then square the total amplitude to compute the intensity. Figures 9*a* and 9*b* show the acoustic intensity images from one bounce and two bounces, respectively. Figures 9*c* and 9*d* show the intensity images with incoherent and coherent sums of Figure 9*a* and 9*b*, respectively. The mean intensity increases by a factor of 2 after the incoherent sum as expected. The mean intensity increases by a factor of about 3 after the coherent sum. The contrast of sunspots remains the same after the incoherent sum. But the contrast of the preceding sunspot increases from 16% to 22% after the coherent sum.

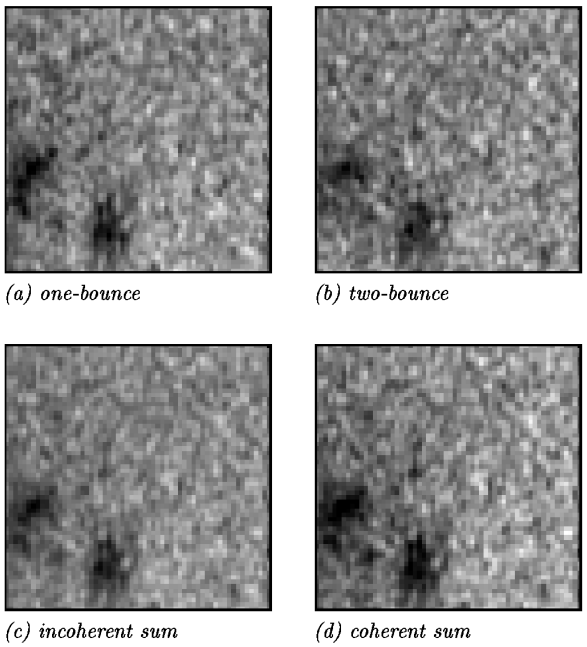

FIG. 9.—Comparison of images constructed with different bounces. (*a*, *b*) Acoustic intensity images from one bounce and two bounces, respectively. (*c*, *d*) Intensity images with incoherent and coherent sum of (*a*) and (*b*), respectively.

5.9. *Cancellation of Signals from Points Other Than the Target Point*

The wave amplitude that we observe at each point on the solar surface includes signals from all other points in the Sun, not just the target point. The key for the success of acoustic imaging depends on the cancellation or minimization of the signals from the points other than the target point in the phased summation. This cancellation is similar to the destructive interference in optics. Detailed theoretical study is required to quantify the degree of cancellation, given the peculiar nature of the solar interior: the steep sound-speed gradient, multiple reflections, and relatively long wavelengths compared to the scale of the phased-array–target system.

Here we give a simple estimate for the signal left over from the incomplete cancellation. For a target point on the surface, the p-mode oscillations with the same ω/l can be decomposed into ingoing and outgoing components, $a_i\Psi(t + \Delta/u) + a_o\Psi(t - \Delta/u)$, where Δ is the angular distance from the target point, u is the horizontal group velocity (depending on ω/l only), and a_i and a_o are the amplitudes of ingoing and outgoing components, respectively. If we apply the phased summation with the time-distance curve, $t = \Delta/u$, to construct the signal at the target point ($\Delta = 0$) at $t = 0$, the contribution of the outgoing component is $\Psi(0)$, which is the signal at $\Delta = 0$ at $t = 0$; this is what we intend to measure. The contribution of the ingoing component is $\Psi(2\Delta/u)$, which is the signal at 2Δ at $t = 0$. If we sum over all ω/l, the contribution of the ingoing component equals the summation of the observed signal in an annulus whose size is twice the collecting annulus. This is the signal left over from the incomplete cancellation. This leftover signal may contribute to the spatial fluctuations of the quiet Sun in the constructed images.

5.10. *Limit of the Focal Depth*

In principle, phased summation can be carried out for a target point at any focal depth. However, at deeper focal depths, fewer modes, only those at lower l, can penetrate into the focal depth: $l_{\max}$ decreases. The signal-to-noise ratio of the constructed acoustic intensity will become smaller, and the spatial resolution will become poorer. Thus there may be a practical limit for the focal depth beyond which this method becomes useless.

5.11. *Phase*

The time series of constructed amplitude contains information on frequency, intensity, and phase. In this paper we mainly present the results from intensity. But the phase can provide much information about the solar interior and atmosphere. Here we give two examples. First, as we have mentioned, the phase of the p-modes advances about 1 minute after the journey of one bounce. This phase shift depends upon the properties of the region near the upper reflection layer of the p-modes (Jefferies et al. 1994). More detailed study with better temporal resolution and a variety of wavelength and frequency bands may provide more information on the properties of the photosphere and chromosphere. Second, we can also compute the cross-correlation between the time series constructed by ingoing waves and that constructed by outgoing waves (Lindsey & Braun 1997). We found that the phase shift between the ingoing and outgoing time series in the active region is different from that in the quiet Sun. This result was present-

ed in another paper (Chen et al. 1998). The phase shift is caused by the change in travel time in the magnetic regions. The time-distance curve used here is derived from the quiet Sun. As discussed in § 5.6, a change in travel time, $\delta\tau$, will cause the time series of constructed amplitude to be shifted by $\delta\tau$. This shift can be detected in the phase measurement. The causes of the change in travel time could be (1) mass flow, (2) perturbation of sound speed, (3) perturbation of acoustic cutoff frequency, and (4) magnetic field (Duvall et al. 1996; Kosovichev & Duvall 1997). Finally, we should mention that the phase information has a better vertical spatial resolution than intensity because the phase information is derived from the whole time series of the constructed amplitude while the intensity is computed by adding the time series of squared amplitude as discussed in § 5.6.

We thank D. Braun and the referee C. Lindsey for their insightful comments. D. Y. C., H. K. C., M. T. S., H. R. C., S. J. Y., and the TON project were supported by the National Science Council of the Republic of China under grants NSC-87-2112-M-007-044, NSC-87-2122-M-007-050, and NSC-87-2112-M-182-003. B. L. was supported by NASA grant NAG5-4941.

REFERENCES

Bogdan, T. J., Braun, D. C., Lite, B. W., & Thomas, J. H. 1997, ApJ, 492, 379
Bogdan, T. J., Brown, T. B., Lite, B. W., & Thomas, J. H. 1993, ApJ, 406, 723
Braun, D. C. 1997, ApJ, 487, 447
Braun, D. C., Duvall, T. L., Jr., & LaBonte, B. J. 1987, ApJ, 319, L27
Braun, D. C., Lindsey, C., Fan, Y., & Fagan, M. 1998, ApJ, 502, 968
Braun, D. C., Lindsey, C., Fan, Y., & Jefferies, S. M. 1992, ApJ, 392, 739
Chang, H.-K., Chou, D.-Y., LaBonte, B., & the TON Team. 1997, Nature, 389, 825 (Paper I)
Chen, H.-R., Chou, D.-Y., & the TON Team. 1997, ApJ, 490, 452
Chen, H.-R., Chou, D.-Y., Chang, H.-K., Sun, M.-T., Yeh, S.-J, LaBonte, B., & the TON Team. 1998, ApJ, 501, L139
Chen, K.-R., Chou, D.-Y., & the TON Team. 1996, ApJ, 465, 985
Chou, D.-Y., et al. 1995, Sol. Phys., 160, 237
Chou, D.-Y., Chang, H.-K., Chen, H.-R., LaBonte, B., Sun, M.-T., Yeh, S.-J., & the TON Team. 1998, in *SOHO* 6/GONG 98 Workshop, Structure and Dynamics of the Interior of the Sun and Sun-like Stars, ed. S. Korzennik et al. (ESA SP-418; Paris: ESA),597
D'Silva, S., & Duvall, T. L., Jr. 1995, ApJ, 438, 454
D'Silva, S., Duvall, T. L., Jr., Jefferies, S. M., & Harvey, J. W. 1996, ApJ, 471, 1030
Duvall, T. L., Jr. 1982, Nature, 300, 242
Duvall, T. L., Jr., D'Silva, S., Jefferies, S. M., Harvey, J. W., & Schou, J. 1996, Nature, 379, 235.
Duvall, T. L., Jr., Jefferies, S. M., Harvey, J. W., & Pomoerantz, M. A. 1993, Nature, 362 430
Hill, F. 1988, ApJ, 333, 996
Jefferies, S. M., Osaki, Y., Shibahashi, H., Duvall, T. L., Jr., Harvey, J. W., & Pomoerantz, M. A. 1994, ApJ, 434 795
Kosovichev, A. G. 1996, ApJ, 461, L55
Kosovichev, A. G., & Duvall, T. L., Jr. 1997, in Solar Convection and Oscillations and Their Relationship, ed. J. Christensen-Dalsgaard 7 F. Pijpers (Dordrecht: Kluwer), 241
Libbrecht, K. G., & Morrow, C. A. 1991, in Solar Interior and Atmosphere, ed. A. N. Cox et al. (Tucson: Univ. Arizona Press), 479
Lindsey, C., & Braun, D. C. 1990, Sol. Phys., 126, 101
———. 1997, ApJ, 485, 895
Nakajima, H., et al. 1980, PASJ, 32, 639
Roddier, F. 1975, CR Acad. Sci. Paris, 281, 93
Scherrer, P. H. 1995, in Proc. Fourth *SOHO* Workshop on Helioseismology, ed. V. Domingo et al. (ESA SP-376; Paris: ESA), 97
Wild, J. P. 1961, Proc. R. Soc. London A, 262, 84
Woodard, M. F. 1997, ApJ, 485, 890